Fully Automated CTC Detection, Segmentation and Classification for Multi-Channel IF Imaging

Evan Schwab, Bharat Annaldas, Nisha Ramesh, Anna Lundberg, Vishal Shelke, Xinran Xu, Cole Gilbertson, Jiyun Byun, Ernest T. Lam

Epic Sciences, San Diego, CA, USA

Abstract. Liquid biopsies (eg., blood draws) offer a less invasive and non-localized alternative to tissue biopsies for monitoring the progression of metastatic breast cancer (mBCa). Immunofluoresence (IF) microscopy is a tool to image and analyze millions of blood cells in a patient sample. By detecting and genetically sequencing circulating tumor cells (CTCs) in the blood, personalized treatment plans are achievable for various cancer subtypes. However, CTCs are rare (about 1 in 2M), making manual CTC detection very difficult. In addition, clinicians rely on quantitative cellular biomarkers to manually classify CTCs. This requires prior tasks of cell detection, segmentation and feature extraction. To assist clinicians, we have developed a fully automated machine learning-based production-level pipeline to efficiently detect, segment and classify CTCs in multi-channel IF images. We achieve over 99% sensitivity and 97% specificity on 9,533 cells from 15 mBCa patients. Our pipeline has been successfully deployed on real mBCa patients, reducing a patient average of 14M detected cells to only 335 CTC candidates for manual review.

Keywords: Metastatic Breast Cancer \cdot IF Imaging \cdot CTCs \cdot Detection

1 Introduction

Liquid biopsies (eg., blood draws) offer a less invasive and non-localized alternative to tissue biopsies for a more continuous monitoring of metastatic breast cancer (mBCa). Immunofluoresence (IF) microscopy is a tool to image and analyze millions of cells in a sample of blood. Circulating tumor cells (CTCs) in the blood are indicative of metastasis and the combination of protein biomarker and single-cell genetic analyses of CTCs provides clinicians with a comprehensive cancer profile for mBCa patients from a single blood draw [16,18].

In mBCa patients, CTCs average 1 in every 2M cells [18], motivating the need for machine learning (ML) to reduce the burden of manual classification by automatically detecting and classifying CTCs. Deep learning has been developed for classifying CTCs in multiple IF modalities [1,2,8,12,15,20,21]. However, these methods fall short of providing a fully automated pipeline to detect and classify CTCs to present for manual review. Furthermore, deep learning loses the utility and interpretability of biomarker features, which clinicians already rely on for manual classification.

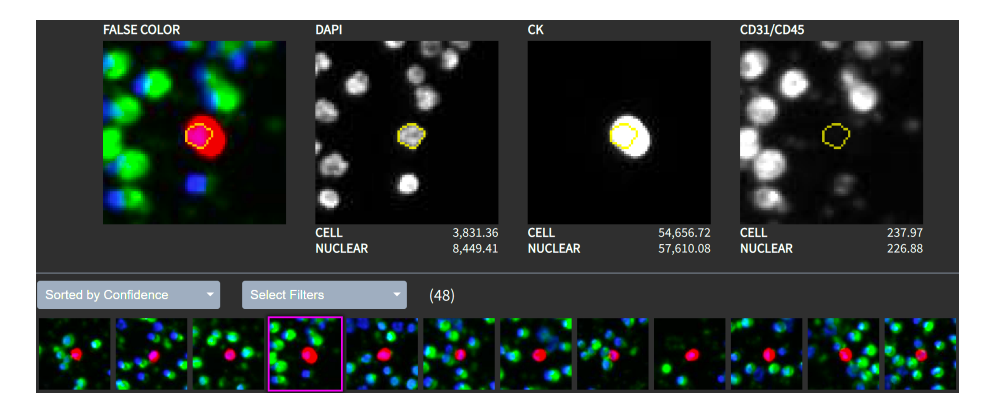


Fig. 1: Example user interface of ML classified CTC candidates output by our pipeline and presented to clinicians (bottom row thumbnails). One thumbnail is selected for review and cell and nuclear MFI values reported per channel. The yellow nuclear mask is overlayed on each channel and the color composite.

In this work, we have developed a fully automated ML-based production-level pipeline to efficiently detect, segment, and classify mBCa CTCs in multi-channel IF images to present to clinicians for final confirmation and genetic sequencing. Our automated pipeline, which we call **BR**east cancer **Imaging Algorithm** (BRIA), combines image processing, deep learning and interpretable feature-based ML. BRIA has been fully deployed at Epic Sciences within a comprehensive clinical workflow that integrates patient sample collection, slide preparation, fluorescence scanning, cloud-based analysis using the proposed pipeline, database management, quality control, and reporting through a proprietary clinical viewer that interacts with data sources through an API.

In Sec. 2 we provide a background on IF imaging and the clinical workflow. Then, in Sec. 3 we present each component of the BRIA pipeline and share our ground truth labeling and experimental results in Sec. 4.

2 Background

Widefield fluorescence microscopy is an IF imaging technique used to capture 2D images of blood samples collected on whole slides [10,19]. Fluorescent dyes are applied in an assay system to capture specific biomarkers of interest and are digitized in multiple imaging channels. At Epic Sciences, we have developed a clinical diagnostic test for mBCa, called DefineMBC, which uses IF imaging as one of the core components for protein biomarker expression analysis. The DefineMBC assay includes DAPI, CK, and CD45/31 channels which are designed to visualize cell components and provide inclusionary and exclusionary biomarkers for CTCs. The DAPI stain (4',6-diamidino-2-phenylindole) is used to highlight

¹ BRIA is agnostic to additional BCa biomarker channels like HER2 or ER.

the nucleus of the cell. The CK stain (Cytokeratin) is an indicator of CTCs and $CD45/31^2$ is an indicator of non-CTCs like white blood cells. Therefore, high CK and low CD45/31 values are indicative of CTCs (see Fig. 2 for examples).

These channel values are summarized using statistical features such as the mean florescence intensity (MFI), ie. the average pixel intensity within an object like the cell or nucleus, for each channel (e.g., Nuclear CK MFI). To compute these features, each individual cell on a slide of roughly 3M cells must be detected and cropped as individual thumbnail images. Then the cell and nucleus need to be segmented to compute MFIs for each channel. In the absence of ML, the standard practice to classify CTCs is to first apply biomarker thresholds (eg. Nuclear CK MFI > 269 and Nuclear CD45/31 MFI \leq 3000, etc.) to filter 99% of non-CTCs and artefacts in our data. However, validating biomarker thresholds is a challenging task and clinicians are still left with 10's of thousands of CTC candidates per patient to sort through.

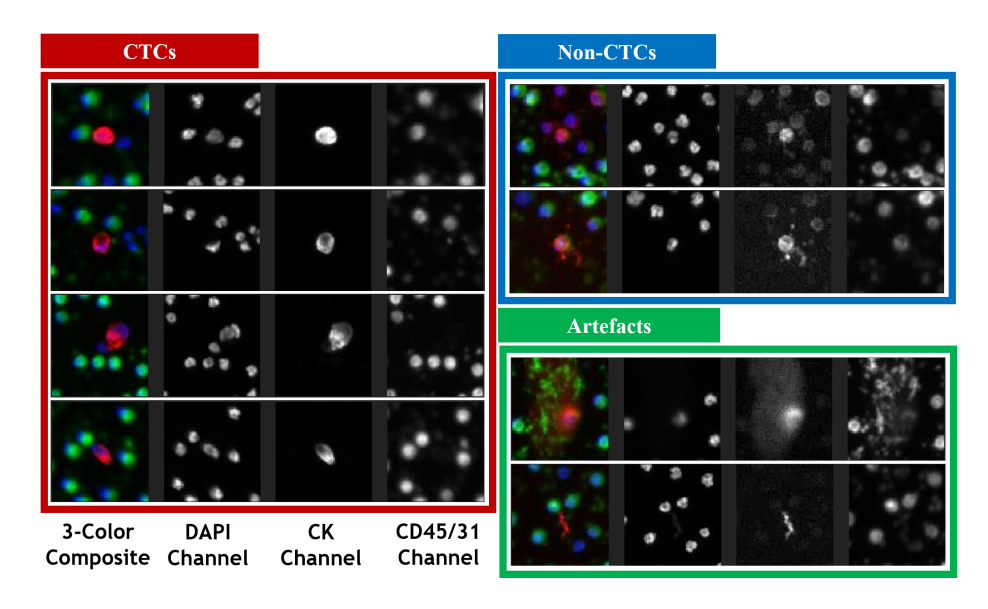


Fig. 2: Example CTCs, non-CTCs, and artefacts in 3-channel IF images with a color composite. CTCs have prominent CK signal and low CD45/31. Some Non-CTCs are visually similar which makes manual classification difficult.

Within this workflow, clinicians manually classify CTCs based on MFI values and the visual inspection of features like cell size, shape, texture and other biomarkers. Because clinicians already rely heuristically on a list of qualitative

² Cluster of differentiation (CD) 31 is a protein associated with white blood cells and endothelial cells. CD 45 is a protein marker of leukocyte lineage.

cellular features, we are motivated to quantify these biomarkers and utilize interpretable feature-based ML instead of deep learning to classify CTCs.

The BRIA pipeline assists clinicians by automating these steps of cell detection, nuclear and cell segmentation, feature extraction and CTC classification to present CTC candidates to clinicians for final review. Figure 1 shows a user interface of CTC candidates presented to clinicians for manual review. For this slide example, the pipeline reduced 3M total cells to 48 CTC candidates instead of what would be 10s of thousands of candidates to sort through.

3 Methods

We outline the main steps of the BRIA pipeline leading up to CTC classification in Sec 3.1 cell detection, 3.2 nucleus segmentation, 3.3 cell segmentation, and 3.4 feature extraction. These steps are also required for manual classification in the absence of an ML CTC classifier. See Figure 3 for a visual overview.

3.1 Cell Detection

The first step of BRIA is to efficiently detect each individual cell center and crop thumbnail images for each cell. Whole slides are too large to image fully and so a grid of 588 (14×42) fields of view (FOVs) of size 2040×2040 pixels are imaged and processed in parallel and stitched together. We compared three classical cell detection methods including watershed, radial symmetry [11] and the Laplacian of Gaussian (LoG) [14]. These are applied to the DAPI channel which highlights the nucleus of each cell (CTCs and non-CTCs alike).

For validation, the centroid coordinates of 24,110 cells from 5 FOVs were manually identified. We measured performance based on the cell count output by the detection algorithm as well as the average distance between the ground truth and estimated centroids. With an exhaustive parameter search, the best performing algorithm was the LoG with cell count F1 score of 0.997 and a 1.12 μ m average distance between estimated and ground truth centroids. This is an acceptable error compared to the average radius of a cell nucleus of about 5 μ m and whole cell size of up to 15 μ m. Small 24×24 pixel thumbnail images are cropped around the centroids based on the average size of nuclei. In total, our cell detection algorithm takes 10 min to detect \sim 3M cells from a single slide.

3.2 Nuclear Segmentation

Once a cell is detected, segmentation of the nucleus is important for extracting features like nuclear MFI for each channel. Since the DAPI channel is already designed to highlight nuclei, nuclear segmentation can be accomplished with classical image processing. Given each thumbnail image, we compute the normal vector field of each pixel to the center and the gradient vector field. These two fields are multiplied using a Gaussian weighted dot product with a radius parameter output by the detection algorithm. This results in a transformed image

that isolates the cell of interest. We compared the watershed method and Otsu's method [7] applied the transformed image to segment the nucleus.

To evaluate performance, the nuclei of the same set of 24,110 cells that were used for the cell detection ground truth were also manually segmented by 40 expert annotators. On a sample of 25 nuclei, we used the Simultaneous Truth and Performance Level Estimation (STAPLE) [17] to measure the concordance between annotators and found 93% sensitivity for segmenting the nucleus correctly. Watershed achieved F1=0.83 while Otsu's method achieved F1=0.934 which is a good performance in comparison to human annotators. With parallelization the nuclear segmentation step takes an average of 10 min per slide.

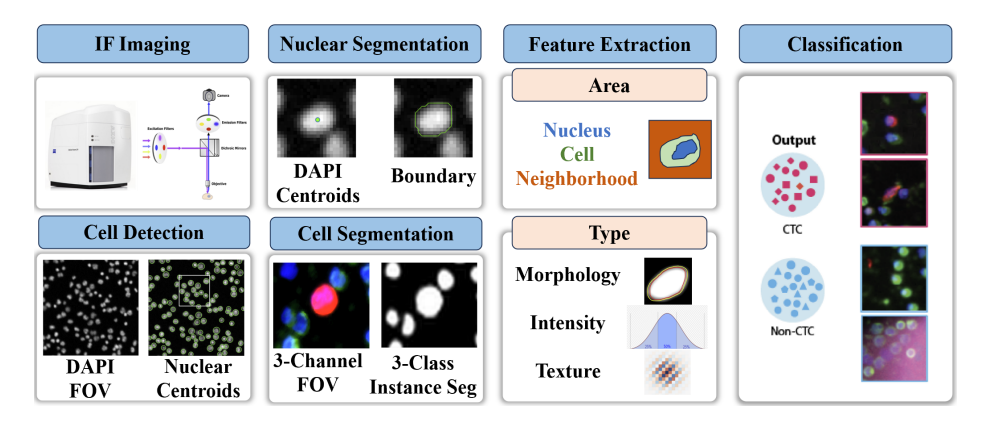


Fig. 3: BRIA Pipeline Overview. After IF image acquisition and slide processing, the main algorithmic steps include Cell Detection, Nuclear and Cell Segmentation, Feature Extraction, and CTC Classification.

3.3 Cell Segmentation

For whole cell segmentation we utilize all three IF channels to account for signal variation across each channel for both CTCs and non-CTCs alike. To address the scarcity of CTCs in our data, simulated montages of CTCs are created to increase their occurrence by placing manually segmented CTCs at randomly generated coordinates on a simulated background image based on real IF images.

We utilize a 3-channel U-Net [9] to segment cells within overlapping 512×512 image patches within each FOV. Overlap was enforced to avoid cutting cells at the edge of a patch. To accelerate this process we use our cell detection output to discard patches that do not contain any cells. The outputs of the U-Net are pixel-level probability maps for three classes: cell, boundary, and background. Including the boundary as a third class proved useful in separating cell clusters. The probability maps for each overlapping patch are merged into a single FOV by taking the maximum among the cell, boundary, and inverted background

probability maps. Then instance segmentation is performed using watershed to identify the masks of each individual cell. These masks are mapped back to each thumbnail using the cell centroids.

Training was performed on 22 patient slides and 9 CTC montages with a total of 10, 443 manually segmented cells. The STAPLE algorithm was again used to evaluate human level segmentation performance. We gave 10 annotators 1,206 cells (including 165 CTCs) to manually segment and their concordance level was an F1=0.936. In comparison our U-Net achieved a comparable F1=0.933 averaged over 5-fold cross validation of our training set. The best performing parameters were learning rate=0.0001, dropout=0.3, weighted classes, network depth=4, epochs=300, and Adam optimizer. Our algorithm took an average of 126s per FOV and with parallelization, segmentation of an entire slide (588 FOVs, 3M cells) was accomplished in 39 min.

3.4 Feature Extraction

Feature-based ML is important for clinicians to better interpret classification results. Since clinicians already rely on quantitative values like nuclear MFI and visually inspect cell morphology and texture, we are motivated to extract additional morphology, intensity, and texture features from the nucleus, whole cell, and entire thumbnail image. In total we extract 122 features which are summarized with equations in Supp. Table 1.

We extract 8 morphology features, 4 each from the nuclear and cell masks: size, roundness, elongation and the first Hu moment [3], which captures more subtle shape variability. (BCa CTCs are often larger than non-CTCs.) We next compute a total of 44 intensity features from nuclear and cell masks across the three channels: MFI, lower, median, and upper quartiles, interquartile range, as well as Pearson's correlations and Ranked-Weighted Co-Localizations [13] between channels. We also extract CK specific features like CK+ ratio, defined as the number of CK pixels that are greater than a cutoff value, divided by the area of the mask. CTCs will exhibit a higher CK+ ratio. We also compute the mean and standard deviation of pixels in the entire CK channel thumbnail which may help eliminate CK+ artefacts like flares.

Finally, we extract 70 texture features. First, a 32D Gabor feature vector is constructed using the mean and standard deviation of filtered images for 16 parameter combinations: $\theta = 0^{\circ}, 45^{\circ}, 90^{\circ}, 135^{\circ}, \lambda = 0.1, 0.4$, and $\sigma = 1, 3$, selected based on cell size. Gabor features identify frequency changes in an image at various orientations and sizes. This helps to identify small dye-aggregates, flares as well as CTCs in an image. Next, a 32D Laws [4] feature vector is constructed by ordered multiplications of 1D filters L5 (Level), E5 (Edge), S5 (Spot), and R5 (Ripple) to detect spatial patterns. Finally, Local Binary Pattern (LBP) [6] encodes edges, corners, raised areas, and lines. LBP results in a transformed image per channel and we calculate the correlation and normalized mutual information between each channel pair, resulting in 6 final texture features.

4 Experiments

Once cells are detected, segmented and features are extracted using the steps of the pipeline described above, we are ready to collect and label ground truth data to train and evaluate a CTC classifier. The CTC classifier is used to replace the standard rule-based biomarker thresholding and substantially reduce the number of CTC candidates presented to clinicians for final review.

4.1 Ground Truth Data

Ground truth data is collected from 15 mBCa patients using the same cell detection and segmentation steps of the pipeline. From 15 patients, a total of 241,644,731 cells were identified by the cell detection algorithm. Then 99.8% of non-CTCs and artefacts were filtered using the rule-based thresholds described in Section 2 leaving 500,255 CTC candidates presented for manual classification. (Without a CTC classifier, this is the number of candidates clinicians would have to manually review in their workflow.) Ground truth CTCs were labeled by four annotators and subjected to a round of adjudication for consensus. They each labeled a comparable number of non-CTCs and non-cellular artefacts. The

Dataset	Patients	Labeled Samples	\mathbf{CTCs}	Non-CTCs	Artefacts
Training	7	4,680	1,667	1,632	1,381
Verification	5	1,931	340	882	709
Validation	3	2,922	1,221	969	732
Total	15	9,533	3,228	3,483	2,822

Table 1: Summary of class sample counts for each dataset split.

result was 9,533 labeled samples with 3,228 CTCs, 3,483 non-CTCs, and 2,822 artefacts. The ground truth data was split at the patient level into training, verification, and validation sets, stratified by number of CTCs (See Table 1).

4.2 CTC Classifier Training

For CTC classification, we combined the non-CTC and artefacts into a single negative class for binary classification. We evaluated four SVM models, including a linear SVM and three non-linear kernel SVMs: radial basis function (RBF), sigmoid, and polynomial. To optimize the classifier performance, the hyper-parameter tuning of C, γ , and polynomial degree were performed using grid search over 5-fold cross validation. All image features were normalized using min-max normalization fit on the training dataset and applied to the verification and validation sets. For our application, it is imperative for patient outcomes to miss as few CTCs as possible (false negatives). Alternatively, allowing false positive CTC candidates only increases the burden of the manual reviewers. Therefore, optimal performance hinges on maximizing sensitivity while controlling for specificity.

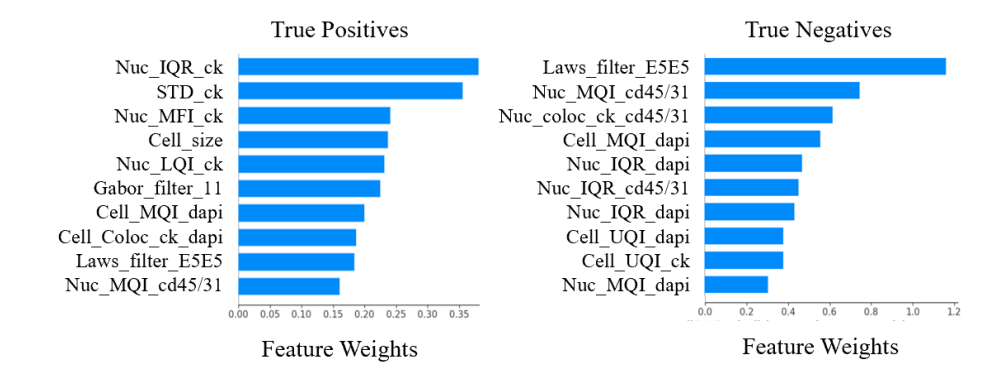


Fig. 4: Top ten features weights for True Positive (CTC) and True Negative (non-CTC/artefact) classes using SHapley Additive exPlanations (SHAP) [5] averaged over 100 random samples per class in the verification set. (Note: Nuc_IQR_ck is the inter-quartile range (IQR) of pixels in the nucleus (nuc) in CK; STD_ck is the standard deviation of CK; Cell_Coloc_ck_dapi is the co-localization of pixels between CK and DAPI within the cell. See Supp. Table 1 for feature definitions.)

Dataset	True Pos.	True Neg.	False Pos.	False Neg.	Sens.	Spec.	Acc.
Training	1,667	3,007	6	0	100%	99.8%	99.9%
Verification	340	1,571	20	0	100%	98.7%	99.0%
Validation	1,210	1,648	53	11	99.1%	96.9%	97.8%

Table 2: Summary of True Positive, True Negative, False Positive, False Negative counts and Sensitivity, Specificity, and Accuracy for each dataset split.

4.3 Results

The SVM with RBF Kernel and hyper-parameters of C=10 and $\gamma=1$ scored the highest average accuracy across the 5 folds. The chosen model was retrained on the complete training set and a 0.3 probability threshold was selected to maintain 100% sensitivity on the training and verification sets with greater than 98% specificity. Of the 26 total false positives in the training and verification sets, 8 were actually Non-CTCs and 18 were determined to be artefacts. Since artefacts are typically easier to inspect by humans this majority of false positives further alleviates the manual review of CTC candidates. We then applied our model to the hold-out validation set and achieved over 99% sensitivity and 97% specificity. See Table 2 for these results.

The ranked feature weights in Fig. 4 indicate that CK intensity features are most important for the CTC class while DAPI and CD45/31 features are more useful for classifying non-CTCs/artefacts. This result coincides with clinical importance of CK in classifying CTCs and can be used for additional interpretation by clinicians.

Finally, we applied BRIA on the full patient data of the combined training and verification sets. With a total of 12 patients, 171M cells were detected (avg. 14M per patient). By biomarker thresholding, 401,608 CTC candidates would have been presented for manual review. In contrast, our ML CTC classifier achieved a $100\times$ reduction for a total of 4,019 CTC candidates (avg. 335 per patient) of which 2,007 are known to be true positive CTCs. Because we achieved 100% sensitivity in the combined training and verification sets, we know that no CTCs were missed on the full patient data. This showcases the true clinical value of our ML-based pipeline to substantially reduce manual workloads.

The BRIA pipeline is configured to leverage AWS Batch jobs that run in parallel, enabling the simultaneous analysis of multiple slides. Each slide takes an average of 90 minutes to complete the analysis. The pipeline requires 32 GB of memory and up to 12 GB of temporary storage for decompressed TIFF image files, while the analysis output files, including slide QC, identified CTC MFI values in JSON format, and cell thumbnails as PNG images, require less than 50 MB of S3 storage.

5 Conclusion

In conclusion, we have demonstrated the clinical utility of our fully automated BRIA pipeline for detection, segmentation, feature extraction, and classification of mBCa CTCs in multi-channel IF imaging. This work is important to deliver patient-specific profiles for mBCa by assisting clinicians in detecting the rare occurrences of CTCs in liquid biopsies. Validated on a hold-out set with over 99% sensitivity our CTC classifier detects nearly all CTCs while reducing substantial burden by presenting 100x fewer candidates for manual confirmation. With BRIA in production, future efforts will focus on continuous learning to monitor and maintain performance of CTC classification over time and expansion to additional cancer types for additional generalization and validation.

Acknowledgments. We thank our ground truth labeling teams, our medical director and the Assay Development, MTT and Clinical groups at Epic Sciences for their support in this work.

Disclosure of Interests. The authors are current or past employees of Epic Sciences and may own company stock options.

References

- Guo, Z., Lin, X., Hui, Y., Wang, J., Zhang, Q., Kong, F.: Circulating tumor cell identification based on deep learning. Frontiers in Oncology 12, 843879 (2022)
- 2. Hashimoto, K., Kamiya, T., Li, G., Yoneda, K., Tanaka, F.: Automatic identification of tumor cells for circulating tumor cells by convolutional neural networks. International Journal of Innovative Computing, Information and Control 19(1) (2023)

- Hu, M.K.: Visual Pattern Recognition by Moment Invariants. In: IRE Trans. Info. Theory. vol. IT-8, pp. 179–187 (January 1962)
- 4. Laws, K.: Texture Image Segmentation (January 1980)
- Lundberg, S.M., Lee, S.I.: A unified approach to interpreting model predictions. In: Guyon, I., Luxburg, U.V., Bengio, S., Wallach, H., Fergus, R., Vishwanathan, S., Garnett, R. (eds.) Advances in Neural Information Processing Systems 30, pp. 4765–4774. Curran Associates, Inc. (2017)
- 6. Ojala, T., Pietikäinen, M., Harwood, D.: A comparative study of texture measures with classification based on featured distributions. Pattern recognition **29**(1), 51–59 (1996)
- Otsu, N.: A threshold selection method from gray level histograms. IEEE Trans. Systems, Man and Cybernetics 9, 62–66 (Mar 1979)
- 8. Park, J., Ha, S., Kim, J., Song, J.W., Hyun, K.A., Kamiya, T., Jung, H.I.: Classification of circulating tumor cell clusters by morphological characteristics using convolutional neural network-support vector machine. Sensors and Actuators B: Chemical 401, 134896 (2024)
- Ronneberger, O., P.Fischer, Brox, T.: U-net: Convolutional networks for biomedical image segmentation. In: Medical Image Computing and Computer-Assisted Intervention (MICCAI). LNCS, vol. 9351, pp. 234–241. Springer (2015)
- Scher, H., Armstrong, A., Schonhoft, J., Gill, A., Zhao, J., Barnett, E., Carbone, E., Lu, J., Antonarakis, E., Luo, J., et al.: Development and validation of circulating tumour cell enumeration (Epic Sciences) as a prognostic biomarker in men with metastatic castration-resistant prostate cancer. European Journal of Cancer 150, 83-94 (2021)
- 11. Schmitt, O., Hasse, M.: Radial symmetries based decomposition of cell clusters in binary and gray level images. Pattern Recognition 41(6), 1905–1923 (Jun 2008)
- 12. Shen, C., Rawal, S., Brown, R., Zhou, H., Agarwal, A., Watson, M.A., Cote, R.J., Yang, C.: Automatic detection of circulating tumor cells and cancer associated fibroblasts using deep learning. Scientific reports 13(1), 5708 (2023)
- Singan, V.R.: Dual channel rank-based intensity weighting for quantitative colocalization of microscopy images. BMC Bioinformatics 12, 1471–2105 (Oct 2011)
- 14. Stegmaier, J., Otte, J.C., Kobitski, A., Bartschat, A., Garcia, A., Nienhaus, G.U., Strähle, U., Mikut, R.: Fast segmentation of stained nuclei in terabyte-scale, time resolved 3d microscopy image stacks. PLoS ONE **9**(2), e90036 (02 2014)
- 15. Tsuji, K., Lu, H., Tan, J.K., Kim, H., Yoneda, K., Tanaka, F.: Detection of circulating tumor cells in fluorescence microscopy images based on ann classifier. Mobile Networks and Applications 25, 1042–1051 (2020)
- Vidlarova, M., Rehulkova, A., Stejskal, P., Prokopova, A., Slavik, H., Hajduch, M., Srovnal, J.: Recent advances in methods for circulating tumor cell detection. International Journal of Molecular Sciences 24(4), 3902 (2023)
- 17. Warfield, S.K., Zou, K.H., Wells, W.M.: Simultaneous truth and performance level estimation (staple): an algorithm for the validation of image segmentation. IEEE transactions on medical imaging **23**(7), 903–921 (2004)
- 18. Werner, S.L., Graf, R.P., Landers, M., Valenta, D.T., Schroeder, M., Greene, S.B., Bales, N., Dittamore, R., Marrinucci, D.: Analytical validation and capabilities of the Epic CTC platform: enrichment-free circulating tumour cell detection and characterization. Journal of Circulating Biomarkers 4, 3 (2015)
- 19. Wilson, M.: Introduction to widefield microscopy (Jun 2017), https://www.leica-microsystems.com/science-lab/introduction-to-widefield-microscopy/

- 20. Zeune, L.L., Boink, Y.E., van Dalum, G., Nanou, A., de Wit, S., Andree, K.C., Swennenhuis, J.F., van Gils, S.A., Terstappen, L.W., Brune, C.: Deep learning of circulating tumour cells. Nature Machine Intelligence 2(2), 124–133 (2020)
- Zhang, A., Zou, Z., Liu, Y., Chen, Y., Yang, Y., Chen, Y., Law, B.N.F.: Automated detection of circulating tumor cells using faster region convolution neural network.
 Journal of Medical Imaging and Health Informatics 9(1), 167–174 (2019)

Supplementary

Object	Feature	Dim	Equation	Description			
Morphology Features (8)							
Nuc/Cell	Size	2	A = O	Area of object O .			
Nuc/Cell	Roundness	2	$R = 4\pi A/C_p^2$	Closeness to a circle.			
				C_p , convex perimeter.			
Nuc/Cell		2	$E = 4A/\pi l_m^2$	Area to major axis l_m			
Nuc/Cell	$1^{\rm st}$ Hu	2	$M_1 = \mu_{2,0} + \mu_{0,2}$	Shape descriptor using			
ruc/ cen	Moment			moments, $\mu_{0,2}, \mu_{2,0}$			
Intensity Features (44)							
Nuc/Cell	MFI	6	$MFI_{ch} = \frac{1}{A} \sum_{p \in O} I_{ch}(p)$	Mean Fluorescence Intensity			
				of object O for channel I_{ch}			
Nuc/Cell	Quartile	24	$LQI_{ch}, MQI_{ch}, UQI_{ch},$	Lower, median, upper, inter-			
	Intensities		$\mathrm{IQR}_{ch}\!=\!\mathrm{UQI}_{ch}\!-\!\mathrm{LQI}_{ch}$	quartile range per channel			
Nuc/Cell	CK+ ratio	2	$CK_+ = I_{ck+}(p)_{p \in O} /A$	Fraction of pixels greater			
				than CK cutoff in object			
Nuc/Cell	Channel	6	Pearson's Correlation	Similarity of pixels between			
rac, con	Correlation			two channels within object			
Nuc/Cell	Channel		Ranked-Weighted	Co-occurrence and corr.			
,	Co-localization		Co-localization	of two channels in object			
CK	Statistics	2	μ_{ck}, σ_{ck}	Mean & Std. Dev. of CK			
Texture Features (70)							
СК	2D Gabor	32	$g(\lambda, \theta, \sigma, \psi, \gamma)$	Frequency patterns in			
	Filters	92		various orientations			
CK	2D Laws	32	Pairs of Level, Edge,	Spatial patterns in			
	Filters	32	Spot, and Ripple filters	various orientations			
DAPI,	LBP		$LBP(p) = \sum_{i} s(n_i - p)2^i$	Local geometric pattern			
CK,	Correlation	6	s(x) = 1 if $x > 1$, else 0	encodings and similarity			
CD45/31	& Mutal Info	20.34	pixel n_i around p	between channel LBPs			

Table 1: Summary of 122 Morphology, Intensity and Texture features extracted from 3-channel IF images (DAPI, CK, CD45/31) within objects of nucleus (Nuc.), cell or full image thumbnail.